Entropy-driven expansion of the thermodynamic stability of compositionally complex spinel oxides

F. Monteverde [a],[*], M. Gaboardi [b],[c]

[a] Institute of Science, Technology and Sustainability for Ceramics – National Research Council of Italy, Italy
[b] Materials Physics Center, CSIC-UPV/EHU, Paseo Manuel de Lardizabal 5, Donostia - San Sebastian 20018, Spain
[c] Chemistry Department, University of Pavia and C.S.G.I., Viale Taramelli, 16, Pavia 27100, Italy

ARTICLE INFO

ABSTRACT

High-entropy ceramics have sparked renewed interest in compositionally complex ceramics since the first introduction in 2015. The kaleidoscopic array of compositions and structures harnessed by this idea has unlocked an unprecedented opportunity to tailor materials for specific applications, including catalysis, thermal barriers, and electrochemical energy storage. Within the family of oxides, a competition exists between rock-salt and spinel structures. The rock-salt structure is highly symmetrical, consisting of a single cation sublattice, while the spinel structure offers more flexibility to accommodate various cations in two distinct sublattices. Herein, we aimed at stabilizing and expanding the thermal stability range of the spinel-structured oxide, successfully synthesizing novel, single-phase, compositionally complex materials by capitalizing on entropy stabilization, all while avoiding the ubiquitous use of nickel and chrome, notorious for their negative environmental impact. The right combination of cations resulted in the synthesis of a seven-metal oxide that is thermally stable up to the remarkable temperature of 1473 K.

1. Introduction

Ever since the breakthrough design and synthesis, in 2004, of new alloys relying on the effective combination of multiple elements in equimolar ratios [1], the use of the term 'high-entropy' (HE) has become increasingly common in materials science [2]. HE alloys (HEAs) are still actively researched today, with a growing number of new systems discovered every year [3,4]. HEAs are solid solutions (SSs) of five or more chemical species with diverse mutual solubility that are stabilized in highly symmetric structures owing to the boost in configurational entropy of mixing, ΔS_{mix}^C. Notwithstanding the simplistic definition of HE for an ideal SS, in more rigorous terms, and according to Brahlek *et al.* [5], the driving force behind the stabilization of a SS often goes beyond ΔS_{mix}^C, and a non-ideal mixing can also result in the formation of a new stable phase, thanks to the role played by additional terms, such as the negative heat of formation (ΔH_f), the thermal entropy of mixing (ΔS_{mix}^{th}), and other terms related to transformations between different structures. In particular, ceramic solid solutions offer more than one anion sublattice, with higher propensity to deform, accommodating

local distortions created by chemical disorder on the metal lattice [6,7]. In all these cases, the more general term compositionally complex (CC) may be preferred. Despite the idea of using entropy to stabilize a CC material is over 50 years old [8], it has only been recently that it has been applied effectively to create stable materials consisting of multiple elements [9]. Non-ideal mixing is the norm for CC materials, not the exception. Simultaneously, achieving an ideal short-range random mixing may not always be uniquely controlled by entropy [10]. The increment in S_{mix}^C leading to the stabilization of a CC material is not the whole story, but it can be essential. In an entropy-stabilized (ES) material, the entropic term must dominate over a positive enthalpic barrier, thus allowing the stabilization of a single-phase above the consolute temperature (T_C) at which the single constituents would normally be partly soluble (see ESI for more details). New interesting properties may arise from the so-called "cocktail effect" [4]. Indeed, very often they are the result of the non-ideal mixing. New systems achieved exploiting this approach as the main driving force for phase stabilization often display unique properties and have sparked exploitation of compositional complexity as a new standard for materials design.

The range of CC materials has been expanded since 2015 to include

* Correspondence to: Institute of Science, Technology and Sustainability for Ceramics, National Research Council of Italy (Via Granarolo 64 I-48018 Faenza(Ra) Italy.
E-mail address: frederic.monteverde@issmc.cnr.it (F. Monteverde).

high entropy oxides (HEOs) [4,7–10] closely followed by CC metal diborides [6,11–16], carbides [17–20] and carbonitrides [21–23]. In this panorama, CC oxides stand out for their excellent performance in dielectrics, sensors, energy storage, catalysis and thermal barrier coatings [24–26]. Structurally, they can occur with different crystal structures, the most recurring ones being rock-salt (*i.e.*, MO, with M: generic cations) and cubic spinels (*i.e.*, M_3O_4). As for the rock-salt (RS) structure, it dominates the landscape of several HE oxides, carbides and carbonitrides thanks to the ability to accommodate different components such as O [7–10,21] C [13,14,17–19] and N [21–23] in the anion sublattice. Nearly all the main metallic species can be inserted in a stable spinel structure, thus offering the opportunity to synthesize a large family of compounds with tunable compositions, cation ordering, electron configurations, and valence states. Such a flexibility makes CC spinel oxides (CCSOs) accessible to a range of diverse applications. The recent literature dedicated to exploring various CCSOs materials (declared as HE) for energy storage is substantial and in continuous expansion [27–53], with one of the most promising applications in anodes for Li-ion batteries, and, of no lesser importance, as catalysts, dielectrics, and as components in high frequency electronic devices, lasers, and sensors [54–99]. However, it is crucial to exercise caution when selecting chemical elements, especially when tackling large-scale applications. Particular attention should be given to avoiding elements with well-documented adverse environmental impacts, such as nickel or chromium. In this regard, Table S1 in the ESI summarizes the recent findings about the synthesis of CCSOs. The latter can generally be described as $(A^{2+})_1^{[t_d]}(B^{3+})_2^{[o_h]}O_4$, with A^{2+} and B^{3+}, respectively, divalent and trivalent cations populating the tetrahedral (t_d) and octahedral (o_h) sub-lattices of a spinel structure, respectively in the 8*a* (0, 0, 0) and 16*d* (5/8, 5/8, 5/8) Wyckoff sites (assuming origin choice 1), while oxygen fills a third different anion sublattice (*i.e.*, the 32*e* site). As a result, the t_d and o_h sublattices in a spinel oxide (SO) can be seen as structurally independent, thus offering a wide range of tuning and laying the foundations for an effective modulation of the properties in a CC spinel-structured material. Species like Ni and Cr, which are known to bring safety issues relative to their processing, handling, and storage, are largely used in relatively 85 % and 65 % of the cases, and in about 55 % of the cases they are used together; the most frequently used species is Fe in relatively 90 % of the cases. It follows that a choice to remove metals like Ni and Cr poses an obstacle when attempting to obtain single-phase SOs. In fact, Ni and Cr find extensive use not only for their multiple valences but also for their tendency to occupy the octahedral site in relation to the so-called octahedral site preference energy (OSPE) which, in crystal field theory, dictates a pronounced ability to form spinels [26].

In the present work, we incrementally doped a CC oxide, deliberately excluding nickel and chromium, to understand how a multi-element spinel with increasing complexity can be produced. In fact, by selectively filling both t_d and o_h sublattices with several different cations, ΔS^C_{mix} can be increased, thus facilitating the stabilization of a CCSO, otherwise hindered by a positive ΔH_f barrier. *Ex situ* laboratory measurements have shown that the range of stability of these spinel-like structures can differ from one composition to another (see Table S1). For some of the CCSOs listed in Table S1, the upper limit of the stability range can be established from the synthesis temperature: this study extensively examines and provides evidence for the entropy-driven stabilization of a seven-cation CCSO above its synthesis temperature.

2. Materials and methods

We started investigating the reaction products of selected calibrated commercial raw oxide powder mixtures, with a varying number of distinct cations (N_C) and compositions (see Table 1. These powder mixtures were allowed to react in air at various temperatures, depending on their composition. The following parent oxides, from ALFA AESAR with a minimum purity of 99.5 wt% or higher and declared particle size
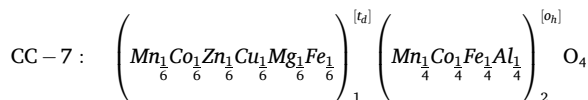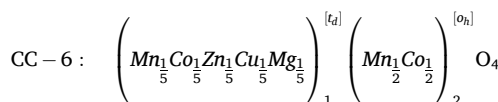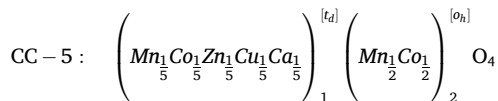
Table 1

Planned compositions of the targeted $(M_i)_3O_4$ spinel oxides investigated in this work and their respective identification number (CC-x, with x=1–7).

CC-x	overall concentration of metals in $(M_i)_3O_4$								
	Mn	Co	Zn	Cu	Ti	Fe	Ca	Mg	Al
1	3/5	3/5	3/5	3/5	3/5	-	-	-	-
2	3/5	3/5	3/5	3/5	-	3/5	-	-	-
3	3/5	3/5	3/5	3/5	-	-	3/5	-	-
4	3/5	3/5	3/5	3/5	-	-	-	3/5	-
5	6/5	6/5	1/5	1/5	-	-	1/5	-	-
6	6/5	6/5	1/5	1/5				1/5	
7	2/3	2/3	1/6	1/6		2/3	-	1/6	1/2

below 10 μm, were used: tetragonal MnO_2 (Pyrolusite, s.g. P4$_2$/*mnm*, ICSD: 643187), cubic Co_3O_4 (s.g. Fd$\bar{3}$m, ICSD: 624573), hexagonal ZnO (Zincite, s.g. P6$_3$*mc*, ICSD: 26170), monoclinic CuO (Tenorite, s.g. C2/*c*, ICSD: 16025), cubic Fe_3O_4 (s.g. Fd$\bar{3}$m, ICSD: 26410), cubic CaO (Lime, s. g. Fm$\bar{3}$m), cubic MgO (Periclase, s.g. Fm$\bar{3}$m, ICSD: 52026), rhombohedral Al_2O_3 (Corundum, s.g. R$\bar{3}$c, ICSD: 857) and tetragonal TiO_2 (Anatase, s.g. I4$_1$/*amd*). The mixtures from CC-1 to CC-4 were designed having equimolar composition.

The non-equimolar CC-5, CC-6, and CC-7 formulations were designed aiming to specific t_d-to-o_h cation distributions, in particular:

$$CC-5: \left(Mn_{\frac{1}{5}}Co_{\frac{1}{5}}Zn_{\frac{1}{5}}Cu_{\frac{1}{5}}Ca_{\frac{1}{5}}\right)_1^{[t_d]}\left(Mn_{\frac{1}{2}}Co_{\frac{1}{2}}\right)_2^{[o_h]}O_4$$

$$CC-6: \left(Mn_{\frac{1}{5}}Co_{\frac{1}{5}}Zn_{\frac{1}{5}}Cu_{\frac{1}{5}}Mg_{\frac{1}{5}}\right)_1^{[t_d]}\left(Mn_{\frac{1}{2}}Co_{\frac{1}{2}}\right)_2^{[o_h]}O_4$$

$$CC-7: \left(Mn_{\frac{1}{6}}Co_{\frac{1}{6}}Zn_{\frac{1}{6}}Cu_{\frac{1}{6}}Mg_{\frac{1}{6}}Fe_{\frac{1}{6}}\right)_1^{[t_d]}\left(Mn_{\frac{1}{4}}Co_{\frac{1}{4}}Fe_{\frac{1}{4}}Al_{\frac{1}{4}}\right)_2^{[o_h]}O_4$$

To further reduce the powder particle size, all the mixtures were mechanically mixed in absolute ethyl alcohol using a planetary ball mill with Mg-stabilized zirconia jar and balls, then dried overnight at 353 K in a ventilated kiln and sieved (250 μm mesh size) to break coarse agglomerates. Prior to in-air high temperature treatment, samples were pelletized onto regular discs with a thickness of about 3 mm using a stainless-steel die (inner diameter 20 mm) and 5 MPa linear applied pressure. Then, discs representative of the CC-x mixtures were selectively fired, choosing a synthesis temperature in the range of 973–1573 K, using a bottom-up loading air furnace, at 15 K/min heating rate. Porous holders made of Mg-stabilized zirconia were used to handle the discs in/out the furnace. All the discs were held for 180 min at the targeted temperature, then quenched in water at room temperature. The as-quenched discs were first pulverized by means of zirconia hard mortar and pestle and finally analyzed by x-ray powder diffraction (XRPD), using Ni-filtered Cu-K_α radiation, on a Bruker D8 Advance diffractometer, to identify the as-quenched crystalline phases. The general classification CC-x-yK was used to identify a CC sample with starting composition (x) dwelled for 180 min at a certain synthesis temperature (yK) before quenching in water.

The as-mixed and unreacted CC-7 oxide mixture was also studied *in-situ* by means of synchrotron XRPD (hereafter sXRPD) using the cylindric furnace setup (coupled to a sliding image plate detector) [100] on the high-resolution MCX beamline at the Elettra synchrotron light-source (Trieste, Italy) [101]. Powder patterns were collected in Debye-Scherrer geometry at 17 keV (λ=0.7293 Å) from 298 to 1273 K in flowing air, at 12 K/min heating rate, acquiring data at steps of 50 K from 323 to 1173 K and 20 K in the last segment, with 3 minutes

dwelling time for temperature stabilization and 2 min accumulation time. A 0.3 mm diameter quartz capillary was filled with few mg of the CC-7 powder mixture and spin horizontally (±90°) with the base of the capillary connected to an oxygen reservoir via an O-ring tight Teflon tube. Integrated patterns were analyzed by means of Rietveld refinement using the GSAS-II suite [102], fitting the lattice and thermal displacement parameters (U$_{iso}$). Isotropic lattice microstrain ($\delta d_{hkl}/d_{hkl}$) and isotropic size broadening were also refined to improve the profile. The instrument profile was calculated using a Si standard (NIST SRM 640*c*) by refining the peaks shape with a pseudo-Voigt (PV) function. A suitable Chebyshev polynomial was employed to simulate the background. The as-synthesized CC-7–1473 K sample was also analyzed *ex situ* at room temperature and at high-resolution in Debye-Scherrer geometry using the 4-axes Huber goniometer of the MCX beamline. The instrument profile of the laboratory XRD diffractometer was also calculated using the same Si standard. The particle density of CC-7–1473 K was determined using a helium pycnometer Micromeritics (AccuPyc II 1340).

Field emission scanning electron microscope (FESEM, $\sum$igma ZEISS, Germany) analyses were carried out to study the microstructure of some as fired samples. Chemical analyses and elemental mapping were also performed using the energy dispersive spectroscopy detector (EDS, Inca Energy 300, Oxford Instruments, UK) installed inside the FESEM. Prior to FESEM-EDS analyses, the samples were coated with a thin C layer. Calorimetry and thermogravimetric data from an un-reacted sample of CC-7 powder mixture were collected using a NETSZSCH model STA 449 F1 Jupiter system in a Pt crucible at 5 K/min in flowing dry air up to 1223 K. The instrumental background was removed, and a suitable asymmetric truncated quadratic function was employed to subtract the experimental baseline.

3. Results

3.1. Exploration of the chemical complexity

The selected four "equimolar" mixtures CC-1 to CC-4 were heat-treated following different programs, setting a maximum temperature ranging from 973 to 1473 K. Under these various cation substitutions, the phase evolution of the initial mixtures at varying synthesis conditions was studied by means of *ex situ* XRPD (see Table 2 and Fig. S2a-*d* in the ESI file). On a relevant note, none of these compositions resulted in a single-phase RS structure. In contrast, formation of multiple phases (MP) was always observed, comprising both SO and RS structures.

The exception to that was sample CC-1–973 K, the only one that showed prevailing single-phase SO structure stabilized after quenching it from 973 K, most likely thanks to the strong spinel-forming ability of Ti [26]. However, single phase stability was also disrupted already at 1073 K, above which other phases were revealed in the powder pattern (see Fig. S2a). Above 1273 K the SO phase was almost extinguished. Following this experiment, we changed the composition, splitting the formerly equiatomic combination of cations into different populations with the idea to selectively occupy the two metal sublattices t_d and o_h. To this end, the initial chemical complexity was reformulated by re-proportioning the spinel-like formers Mn, Co, and Cu, as well as including other species like Fe and Al. Such a change led to more encouraging results. CC-5 was formulated with the idea of sharing the tetrahedral site between Ca and the other metals (Mn, Co, Zn, and Cu) with the octahedral one only split between Mn and Co. The XRPD data showed not-well-formed SO features at 973 K, and other minor peaks, tentatively ascribed to RS phases. At 1173 and 1273 K the SO phase showed better diffraction features, in addition to a secondary phase, but above that temperature the stability was compromised. An encouraging improvement was achieved by replacing Ca with Mg (sample CC-6), obtaining a seemingly single-phase SO stable up to 1273 K (see Fig. S2f), above which phase separation occurred. Eventually, the best result is achieved with composition CC-7, whose diffraction patterns show the formation of a single-phase SO structure, stable even after quenching at 1473 K (see Fig. 1). The use of Al and Mg in formulations containing also Ni is already well documented in [49,61,64,69,78,80]. However, the sole Ni and Cr-free CCSO formulation similar to CC-7 was found by Li *et al.* with the synthesis of $(Zn, Co, Mn, Fe, Al, Mg)_3O_4$, deemed stable up to 1273 K [29].

The thermodynamic stability of CC-7 was investigated at temperatures as high as 1573 K, at which a minor peak, belonging to the RS structure, suggests the upper limit of stability. The CC-7 composition was also part of a broader experimental campaign made to address the effective role of entropy in the stabilization of CC-7 CCSO, which will be discussed later in Section 3.2. A representative FESEM micrograph of sample CC-7–1473 K, as well as a FESEM-EDS elemental mapping through a polished section are displayed in Fig. 2a, showing the hosting matrix, that is, the 7-cations CCSO phase (as strongly suggested by ex situ XRPD), with new features appearing along grain boundaries or as intra-granular segregation. To further the insight, elemental mapping and quantitative line scan were carried out (see, respectively, Fig. 2a and c-i), whose careful evaluation clearly allows to attribute the segregated minority phase to a segregation of a Cu-Co oxide from the CCSO matrix and various metals homogeneously distributed. This agrees with what predicted by the Ellingham diagrams for the oxidation of various metals reported in Figure S3, which confirms that Cu is the metal most prone to oxidation [103] followed in order by Co, Fe, and Mn. The qualitative FESEM-EDS line scan integration confirmed a homogeneous distribution of the cations inside the hosting CC matrix. To broaden the

Table 2
Assessment by ex situ XRPD of the as-quenched products, distinguishing between the formation of multiple phases (MP) and the obtainment of a single-phase spinel oxide (SP-SO).

| CC-x	Maximum temperature of synthesis (K)					
	973	1073	1173	1273	1373	1473
1	SO*	MP	MP	MP	MP	MP
2	MP	MP	MP	MP	MP	MP
3	MP	n/t	MP	MP	MP	MP
4	MP	MP	MP	MP	MP	MP
5	MP	n/t	MP	MP	n/t	MP
6		n/t		SO	MP	MP
7		(ª)		SO	SO	SO*

All samples were dwelled at the maximum temperature for 180 minutes before quenching.

(*) presence of a very weak secondary phase.

ª Temperature range explored in the dedicated multi-stage experiment from 900 to 1573 K. (SO) spinel oxide. (MP) multiple phase.
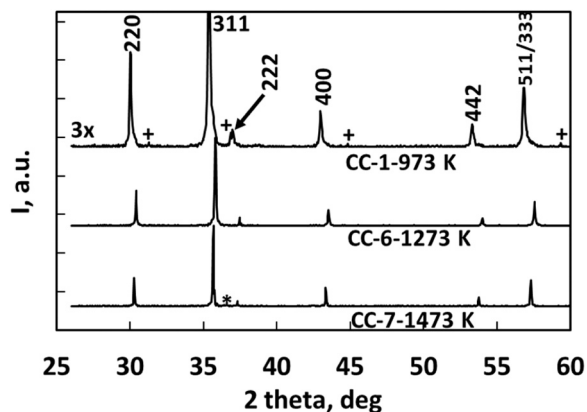
Fig. 1. Ex-situ laboratory XRPD patterns of CC-x samples showing (nearly) single-phase spinel oxide features (indexed). The strongest peak of a rock-salt phase is highlighted by an asterisk only for CC-7–1473 K. The CC-1–973 K full pattern scale is 3x stretched to visualize a minor spinel oxide (+).
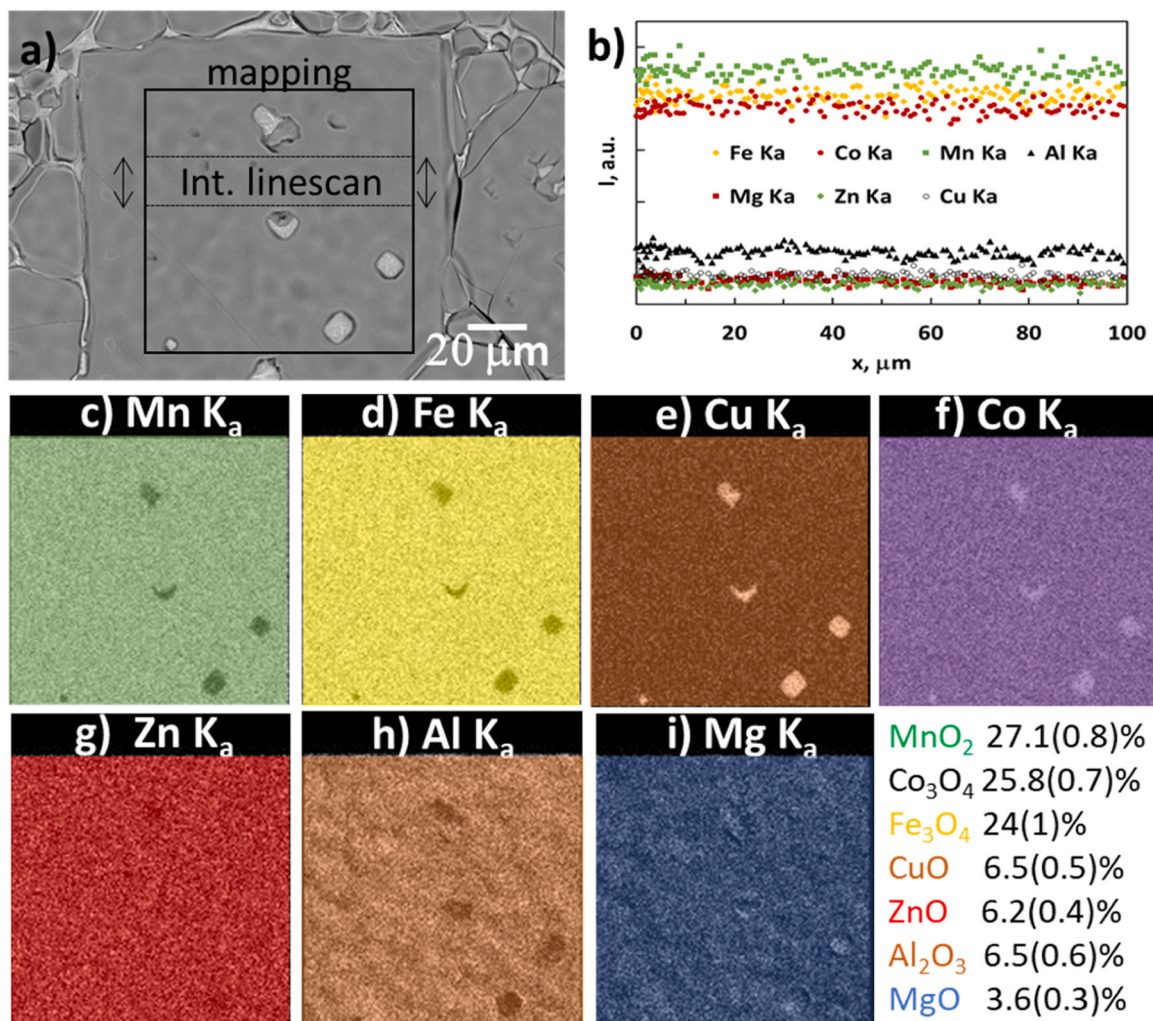
Fig. 2. BSE-FESEM micrograph from a polished surface of CC-7–1473 K. (a) Features with a brighter grey level are Cu-based minority phases along grain boudaries and intragranularly. (b) Linescan integrated over the 20 μm wide band of (a). Average wt % values and standard deviation (between parentheses) are shown at the bottom right corner. (c-i) Elemental mapping relative to the same area.

understanding regarding the chemical nature of the RS phase, additional FESEM-EDS studies are provided in the ESI file with Figure S4 and S5.

The in-situ sXRPD experiment (see Fig. 3) provides insight into the formation process of the final SO phase CC-7, starting from the initial unreacted mixture. Several phase changes occur upon synthesis. As expected, at room temperature the powder pattern is constituted by the superimposition of 7 different oxides. The phase fractions of the as-milled CC-7 mixture were Rietveld refined at room temperature and are reported in Table S2 (ESI). Taking into account the strained status of the heavily milled powders the agreement between the expected values and the calculated ones can be considered acceptable. From room temperature to about 723 K no detectable structural change was observed, apart from the expected thermal expansion (region a in Fig. 3). Region b, from 723 to 823 K, is marked by the appearance of new features at about 11.25 and 15.48°, tentatively ascribed to a new $Ia\bar{3}$ (αMn$_2$O$_3$-like) phase, whose exact composition is hard to predict. At the same time, the simultaneous emergence of a spinel phase stemming from the former Fe$_3$O$_4$ peaks is evident from the increased intensity of the 111, 220, and 311 reflections. It is possible that, at these temperatures, the combined effect of thermal diffusion and expansion of the $Fd\bar{3}m$ lattice of Fe$_3$O$_4$ are sufficient to start the accommodation of more cations from the other oxides (Mn in particular) in the seed of the forming single phase CCSO.

At this stage, the unknown composition of the intermediate $Ia\bar{3}$

phase, the overlapping of peaks belonging to CuO, Al$_2$O$_3$ and MgO, and the continuously changing composition of the final spinel oxide make multi-phase Rietveld refinement rather complex due to strong correlation between variables. However, we can still extract semi-quantitative information from the single-peak fitting of a few isolated reflections, belonging to specific phases. To this end, we fitted the most relevant peaks to pseudo-Voigt functions with intensities as free parameters and positions relative to the cell symmetry (see Fig. 4 and legend).

In region c, from 823 to 923 K we register the complete disappearance of the MnO$_2$ phase. The $Ia\bar{3}$ phase vanishes entirely at 1193 K (end of region e in Fig. 3, and Fig. 4). Meanwhile, the spinel phase peaks dominate the landscape of the powder pattern, whilst the other oxides are progressively consumed. In region e, from 1123 to 1193 K, the newly formed CCSO phase reverse its thermal expansion trend and begins to contract, possibly due to the increasing ionic effect of absorbed Mg from the MgO phase (harder to distinguish from the other phases due to strong peak-overlap). At this stage, Co$_3$O$_4$ and CuO are also being completely absorbed. Region f, from 1193 to 1253 K, sees the complete formation of the CCSO phase and disappearance of any remaining precursors. Finally, above 1253 K (region g), CCSO is hegemonic and stable as single phase with lattice parameter 8.44574(10) Å at the stabilization temperature of 1273 K.
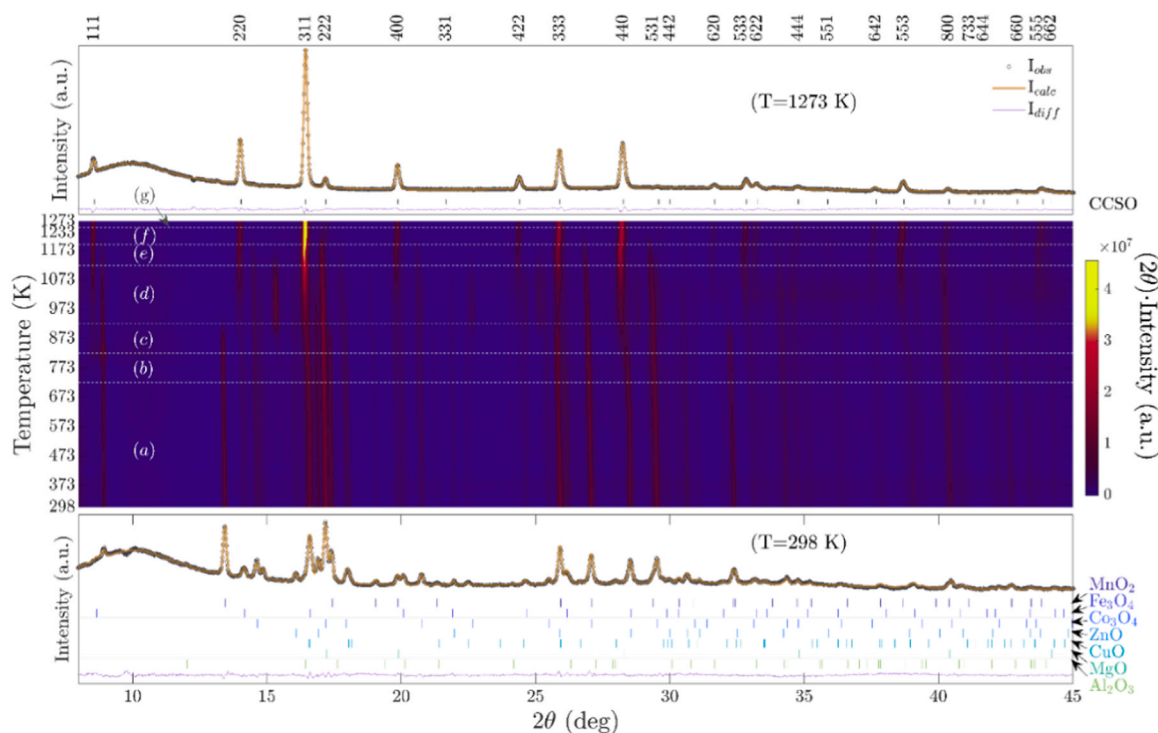
Fig. 3. Middle panel: contour plot of the in-situ synchrotron powder diffraction experiment (λ=0.7293 Å) on CC-7 (Intensity for $2\theta<10°$ were magnified 5 times). Bottom and top panels: Rietveld refinements of powder patterns with phases described by vertical tick marks (see labels on the right) respectively at 298 and 1273 K. (a-g) region of phase change (delimited by horizontal dashed lines), as discussed in the main text. Reflections in the upper panel are also indexed according to the relative hkl indexes for the $Fd\overline{3}m$ symmetry (spinel).
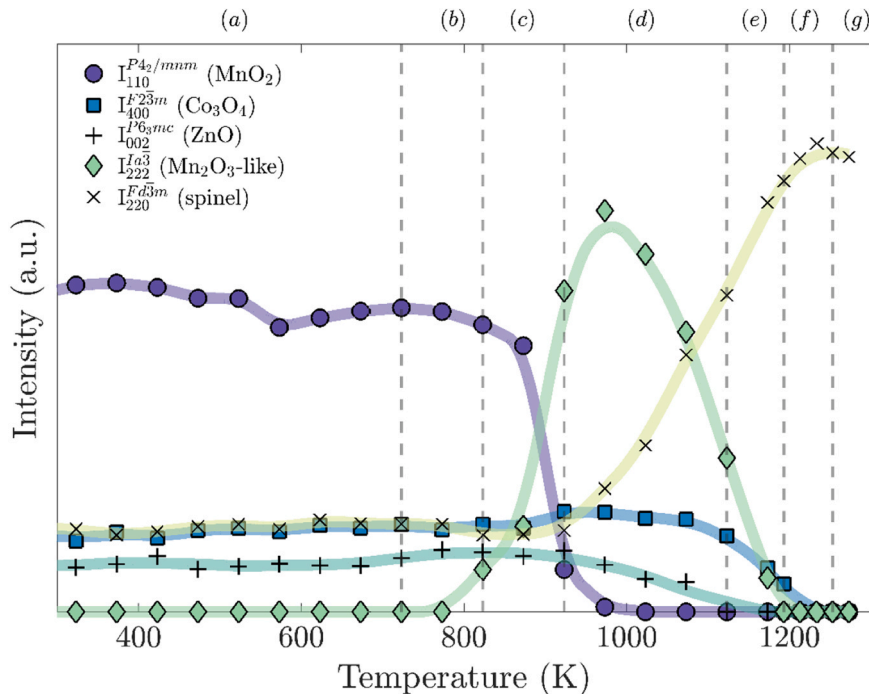

Fig. 4. Normalized intensity of selected reflections belonging to isolated peaks observed during the in-situ experiment. Peaks were fitted to pseudo-Voigt function with intensity as a free parameter and position described by the cell indexed in the legend. The peak defined as $I_{222}^{Ia\overline{3}}$ (JCPDS No. 41–1442) is relative to the transient phase appearing in the range 800–1200 K. $I_{311}^{Fd\overline{3}m}$ highlights the intensity of the reflection formerly belonging to Fe_3O_4 and subsequently merging into the final CCSO. CuO, Al_2O_3, and MgO phases were omitted due to overlapping peaks. Solid lines are a guide to the eye.

3.2. Manipulation of the chemical complexity and entropy stabilization

In light of the previous structural results and chemical analysis, we observed that composition CC-7 resulted in a single-phase CCSO after annealing above 1253 K. However, whether this material also falls within the domain of entropy-stabilization and/or high-entropy is yet to be determined. The consensus around the definition of HE is to have a ΔS_{mix}^{C} boost higher than 1.5 *R,* where R is the universal constant of gas. Equimolarity is frequently utilized to maximize the increase in entropy but is not essential. On the other hand, to qualify as ES, CC-7 should be single phase and display a positive enthalpy counterbalanced by $T\Delta S_{mix}^{C}$ above the temperature of formation.

To shed more light on the entropy stabilization we can start by establishing a correlation between the results obtained from the *in-situ* sXRPD experiment (*cfr.* Fig. 3 and Fig. 4) with the calorimetric (DSC) and thermogravimetric (TGA) data presented in Fig. 5. A net mass loss of about 5.5 % was measured during the whole process. Characteristic TGA and DSC parameters are reported in Table 3, corresponding to the four characteristic events labeled P_0, P_1, P_2, and P_3. Overall, a large background dominates the DSC signal, suggesting a first increase in specific heat, followed by an overall decrease above 900 K. The first exothermic feature in the DSC with onset temperature 459 K (*i.e.*, P_0) is not accompanied by a corresponding (measurable) signal in the TGA curve. In addition, relevant events in the *in-situ* sXRPD powder pattern of Fig. 4 were not observed but only a slight 110 peak intensity change related to the MnO_2 phase. This led to tentatively attribute P_0 to minor changes affecting the long-range structure of MnO_2 before the initiation of more evident changes clearly captured by P_1 peak, though a thorough explanation of the P_0 event was not found yet.

P_1 is interested by a net mass loss, most likely oxygen release, accompanied by a small endothermic peak. The only indication of structural changes in this region is the slight decrease in the MnO_2 110 intensity at about the same temperature. P_2, on the other hand, shows a clear endothermic peak and the largest mass loss of 2.78 %. In fact, CC-7 amounts to more oxygen than that required to reach the final AB_2O_4 stoichiometry. Process P_2 is most likely related to the appearance of an

Table 3

The four main thermodynamic processes (P_N) observed in Fig. 6. Mass loss (ML), corresponding onset (T_{on}), expiring (T_{end}), and peak temperature (T_{max}) as extracted from TGA, as well as DSC onset temperature (T_{DSC}^{on}) and total exchanged heat (ΔH_{DSC}) from DSC analysis.

|	TGA				DSC		
	T_{on} (K)	T_{max} (K)	T_{end} (K)	ML (%)	type	T_{DSC}^{on} (K)	ΔH_{DSC} (J g^{-1})
P_0	/	/	/	/	*exo*	459	-53.5
P_1	550	575	600	0.41	*endo*	567	11.5
P_2	785	870	910	2.78	*endo*	825	113.4
P_3	n/a	1090	1115	0.39	*endo*	1067	293.2

Mn_2O_3-like phase and the onset of the chemical changes involving formation of the first seed of the CCSO phase, occurring with an overall absorption of heat. At this stage, the chemical composition will most likely be richer in Fe and Mn, with the other metals progressively diffusing in the CCSO phase with the increasing temperature. The final mass loss observed in P_3 is small and corresponds with the last endothermic event with onset at 1067 K. This final thermal event corresponds to the initial drop, starting around 1000 K, in diffraction intensities of the remaining ZnO, Co_3O_4, and the Mn_2O_3-like phase (see Fig. 4), ultimately leading to complete formation of the CCSO phase.

The same composition was treated up to 1473 K for 180 min and quenched in water (sample CC-7–1473 K) and further analyzed *ex situ* with high-resolution sXRPD at 298 K. The pattern can be easily indexed to a $Fd\overline{3}m$ cell with cell parameter refined to 8.35371(6) Å (see Fig. 6). For Rietveld refinement we employed the same stoichiometry and cation distribution (i.e., fixed occupancy) designed in the preparation of composition CC-7 (later renamed MOD6:4 in Section 4), constraining the isotropic thermal parameters to equal values for atoms filling equivalent same sites. More details about this structure will be given in Section 4.

The comparison between the lattice parameter of CC-7–1473 K at 298 K compared with that obtained *in-situ* at 1273 K (i.e., 8.44574(10) Å) results in an average coefficient of linear thermal expansion (α_{AV}) of
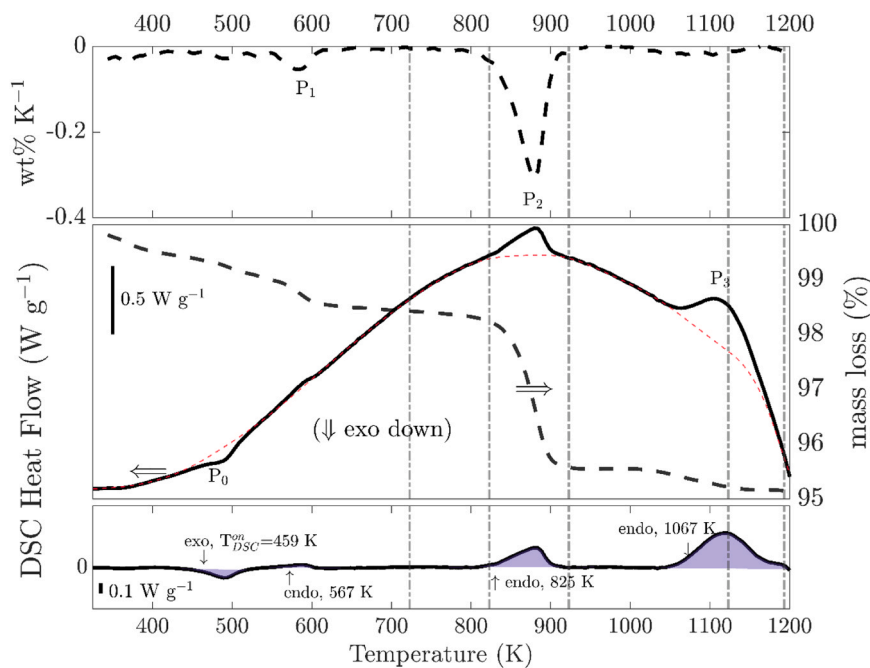
Fig. 5. Thermo-gravimetric analysis of sample CC-7 as a function of the temperature (exo-down, heating rate: 5 K min^{-1}). Central panel: DSC heat flow (black solid line), mass loss (dashed line, right y-axis). The subtracted background is displayed as a red dashed line. Bottom frame: background-subtracted DSC signal (endo and exo processes are emphasized by shaded areas) and their onsets highlighted by arrows. Top panel: relative rate of weight loss, highlighting the most relevant processes (see also Table 3 and main text). Vertical dot-dashed lines mark the main phase-change regions as reported in Fig. 3 and Fig. 4.
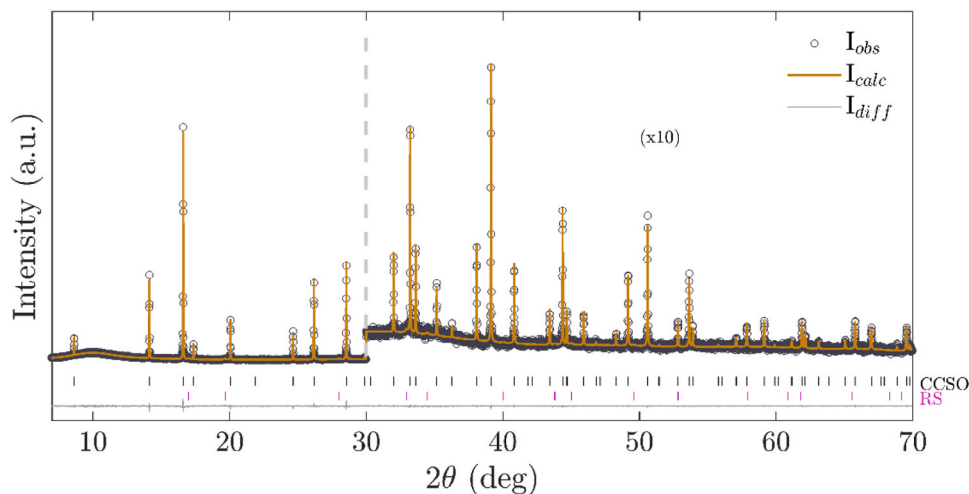
Fig. 6. High-resolution synchrotron powder diffraction data of sample CC-7–1473 K collected at 298 K (I_{obs}) and Rietveld refinement (I_{calc}) using model MOD6:4 (R_{wp} = 7.87 %; g.o.f.=1.19; $I_{diff}=I_{obs}-I_{calc}$; $\delta d/d=0.066(2)$ %). Further information about the model is given in the discussion section. Data at 2θ values higher than 30° are magnified 10 times. Indexed reflections are displayed as vertical tick marks for the spinel-oxide phase (CCSO) and a rock-salt structure (RS).

$1.13 \cdot 10^{-5}$ K^{-1}. A very careful analysis of the powder pattern also reveals the existence of weak features tentatively ascribed to an RS impurity (lattice parameter 4.2540(13) Å). The powder density of CC-7–1473 K, determined via He pycnometry, was 4.94 ± 0.02 $g\ cm^{-3}$, a result that will be later used to strengthen the significance of the structural model adopted to describe the 7-cations CCSO.

To further corroborate the entropy-driven stabilization of this CCSO, we carried out an additional experimental campaign, involving multiple stages. This extended study enabled us to delve deeper into the temperature-dependent reversibility of the material. Several dedicated samples of equivalent composition CC-7 were heat-treated following the temperature scheme reported in Fig. 7 and quenched in water at room temperature. The as-treated samples were then finely ground, and *ex situ* XRPD collected (see Figure S6). Naming of samples follows a sequential number (as subscript) while the upper annealing temperature is reported in Table 4, *e.g.*, t_0 for the specimen quenched in water after 180 min at 900 K. A thorough analysis of the XRPD patterns displayed in Figure S7 reveals a pronounced impact of temperature and annealing time in determining the stabilization of a single-phase CCSO. Sample t_0 shows dominant features of a SO component, accompanied by several peaks originating from unreacted metal oxide moieties. In the XRPD pattern of t_1, a minor residue of Co_3O_4 remains, indicating that this phase is the last oxide to react from the original mixture, as also highlighted by in-situ sXRPD (see). The XRPD patterns of samples quenched within the

Table 4
Refined parameters (errors in parenthesis) of the SO phase (s.g. $Fd\bar{3}m$) observed in the XRPD patterns of Fig. 7. Cell parameters (a), cell volume (V_{XRD}), lattice microstrain ($\delta d/d_{hkl}$), and weighted R-factor of the refinement (R_{wp}). Final temperature (T) and cumulative time are also reported for each step of the ramp.

	T (K)	time (min)	a (Å)	V_{XRD} (Å^3)	$\delta d/d_{hkl}$ (%)	R_{wp} (%)
t_0	900	220	8.3806(4)	588.61(8)	1.93(2)	2.63
t_1	1073	315	8.36767(7)	585.89(1)	1.59(1)	1.36
t_{1b2}	1273	400	8.3319(1)	578.40(2)	0.372(6)	2.2
$t_{2,3}$	900	640	8.34179(7)	580.47(2)	0.705(3)	1.41
t_{3a}	1073	620	8.33816(4)	579.71(1)	0.377(3)	1.27
t_{4a}	1273	760	8.34058(4)	580.214(7)	0.08(1)	1.2
t_4	1273	760	8.33957(5)	580.00(1)	0.36(1)	1.55
t_5	1473	860	8.35275(5)	582.76(1)	0	1.88
t_6	1573	920	8.36240(6)	584.78(1)	0	2.1
t_7	1073	1060	8.35663(6)	583.57(1)	0.134(6)	1.65

range of 1073–1273 K persistently reveal the presence of a single $Fd\bar{3}m$ phase (see t_{1b2}, t_{3a}, t_4, and t_{4a} in Figure S6), suggesting 1273 K as the lower limit of stability. The specimen cooled from 1473 K displays weak features (almost negligible) from a minor RS phase in the powder pattern, indicating 1473 K (or a slightly lower temperature) as the upper limit of thermodynamic stability of the so-formed CCSO (see t_5 in Figure S6). The pattern of the specimen cooled from 1573 K (see t_6 in Figure S6) displays more evident features of the minor RS phase (lattice parameter a=4.2614 Å). The same features are also observed following the last step at 1073 K (t_7 in Figure S6), achieved after cooling from 1573 K, pointing to the irreversible character of the SO-to-RS phase transformation. The alternative thermal pathway $t_{1b,2}$-$t_{2,3}$-t_4 and the XRPD pattern of t_4 was key to prove that the single phase CCSO obtained at 1273 K (see $t_{2,3}$ and t_{3a}) is also thermally reversible and metastable: the thermal reversibility is necessary condition to declare a CC single phase entropy stabilized. In fact, after a 60 min long annealing at 1273 K, the temperature was decreased to 900 K for 180 min, in order to allow any phase transformation with the chance to occur below the temperature of formation, and it then risen to 1273 K for 60 min, to allow re-annealing and assess thermodynamic reversibility. The sample recovered at 900 K showed minor precipitation of MnO_2 and MgO (see $t_{2,3}$ in Figure S6), while the one back-annealed at 1273 K and rapidly quenched displayed again a perfect CCSO phase (t_4). As a result, the consolute temperature (T_C) very likely falls between 900 and 1073 K and the CCSO is metastable, which is also indicative of the stabilizing
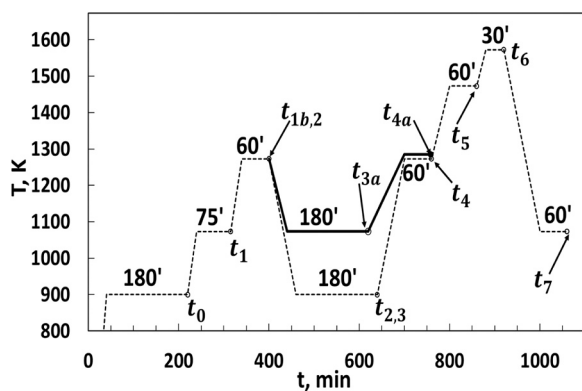
Fig. 7. Scheme of the multi-stage thermal treatment. Dashed and solid lines represent two different thermal paths. Annealing times are specified in minutes. Labels highlight the name of the sample removed at a specific stage of the ramp and quenched in water at room temperature.

effect of entropy at high temperature. The SO phases observed in the XRPD patterns of Figure S6 were fitted via Le Bail analysis for each sample to extract profile and lattice parameters and the results are reported in Table 4. In particular, we highlight the almost matching agreement in lattice parameters between sample t_5 and that measured with high-resolution *ex-situ* sXRPD, respectively 8.35275(5) and 8.35371(6) Å. In addition, in CC ceramics microstrain data can be put into direct relation with the chemical homogeneity [6,104].

In reference to this, we note that the higher level of microstrain observed in t_0, t_1, and $t_{2,3}$ is suggestive of a non-perfectly random distribution of the metal species (see ref. [15]), while samples t_{4a}, t_5, and t_6 display much lower, if not zero, values, indicating a much higher degree of randomness.

4. Discussion

Although increasing the number of components (N_C) under equimolar conditions is a frequently used approach to improve the stability of CC phases, it may not always represent the optimal strategy. The site selection, *i.e.*, the arrangement of cations inside various sub-lattices, can have a significant impact on the energy landscape and structure, particularly when dealing with multiple cation sublattices. Indeed, while equimolarity is the most straightforward way to maximize the entropy in a simple RS structure, in a more complex SO lattice the differentiation between the two possible sites and their respective stabilization energies impose more stringent constraints. An example of this has been recently reported by Coduri *et al.*, who showed that an increasing chemical complexity can be achieved also for non-equimolar formulations [92]. Empirical evidence of this condition also arises from the comparison of our selected mixtures (see Table 2). Of the first four 5-elements equiatomic mixtures, only CC-1 resulted in a nearly single phase CCSO, stable up to 973 K, while non-equiatomic CC-6 and CC-7 CCSOs showed stability up to about 1273 and 1473 K, respectively. Simultaneously, the right choice of metals holds equal significance, as illustrated by the comparison of CC-5 and CC-6 mixtures in the present study. In these cases, substituting Ca with Mg resulted in the formation of a single-phase CCSO very likely owing to the reduced atomic radius of Mg^{2+} compared to Ca^{2+}.

In SOs, the crystal field stabilization energy (CFSE) within the oxygen ligand field is a key factor in determining a cation's preference for either a tetrahedral or octahedral environment. Using the same rationale as Sarkar *et al.*, [72] we calculated the total CFSE's ($CFSE_{tot}$) and correlated them proportionally to ΔH_f (see ESI for method and tabulated CFSE values to compute $CSFE_{tot}$). From data shown in Table 5, we can conclude that the formation of CC-7–1473 K is favored compared to CC-6–1273 K because the former spinel oxide has a lower enthalpy penalty to overcome and a larger entropy boost coming from an higher ΔS_{mix}^C.

As discussed in the previous section, subjecting CC-7 to a treatment at 1273 K awarded us with a new single-phase CCSO, with stability far greater than previously reported structures up to temperatures as high as 1473 K (see Table S1). This result holds particular significance, especially considering the deliberate exclusion of strong spinel formers such as Ni and Cr, intentionally removed for sustainability reasons and supply

chain issues. Additionally, the endothermic nature of the last thermodynamic process and the findings from the multi-stage experimental investigation carried out on CC-7 (cfr. Figure 5 and Figure S6) strongly indicate the occurrence of entropy-driven stabilization. In particular, the $t_{2,3}$-to-t_4 recovery time of 120 min from 900 to 1273 K allowed for the effective redistribution of diverse chemical species leading to quasi-ideal randomness (as suggested by a negligible microstrain value). In a similar report, Rost *et al.* revisited the $Mg_{0.2}Co_{0.2}Ni_{0.2}Cu_{0.2}Zn_{0.2}O$ RS structure and showed a temperature and time dependent full reversibility [105].

What remains to be fully established is whether this entropy-stabilized compositionally complex spinel oxide (ES-CC-SO) also qualifies under the definition of high-entropy ceramics (that is, $\Delta S_{mix}^C > 1.5R$). To this end, under the reasonable assumption that the anion sublattice is occupied exclusively by oxygen, we would need to know the arrangement of cations in the two tetragonal and octahedral sublattices. Using results from elemental analysis (Fig. 2), we confirmed the most probable models of CC-7 and CC-6 against diffraction data (Fig. 6). Table 5 records the models fulfilling elemental analysis and electroneutrality that were employed for this comparison and their relative fitting discrepancies. $CFSE_{tot}$ values were calculated under the hypothesis that cations occupying t_d and o_h sites have, respectively, +2 or +3 as valence. A first fitting was carried out via Le Bail analysis to provide the best lattice, background, and profile parameters. Subsequently, Rietveld refinements were carried out by fixing profile, lattice and chemical occupancy of the metals populating the two sublattices according to the specific model.

The calculated density of MOD6:4 equals to 4.926 $g\,cm^{-3}$ which matches the density obtained with He pycnometry ($\rho_{PICN}^{CC-7-1473K} = 4.94 \pm 0.02$ g/cm³). To put this model into perspective, Fig. 8 displays the increment of $\frac{\Delta S_{mix}^{cat}}{R}$ as a function of the number of cations in the t_d sublattice (N_1) and for a variable number of cations in the o_h site (N_2), where $N_C \leq N_1 + N_2 \leq 2\,N_C$.
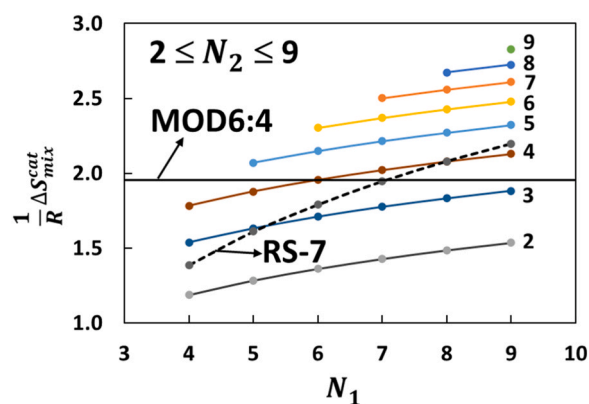

Fig. 8. Dimensionless increment of configurational entropy of mixing for varying (equimolar and fully random) occupancies N_1 and N_2, respectively for the t_d and o_h sublattices of a SO structure. The value calculated for MOD6:4 (spinel with N_1:N_2 equal to 6:4) is displayed as a horizontal solid line. Values calculated for a 7-cations RS structure are also displayed as a dashed line.

Table 5

More relevant models compared with R-factors obtained from Rietveld refinement: $R_{wp}^2 = \sum_i \frac{w_i\left(I_i^{obs} - I_i^{calc}\right)^2}{\sum_i w_i\left(I_i^{obs}\right)^2}$ and goodness of fit ($g.o.f. = \frac{R_{wp}}{R_{exp}}$). Calculated entropy of mixing ΔS_{mix}^{cat} (calculated from Eq. 4) and total CFSE ($CFSE_{tot}$) are also reported.

Model	Sample	t_d sublattice	o_h sublattice	R_{wp} (%)	*g.o.f.*	$\frac{\Delta S_{mix}^{cat}}{R}$	$CFSE_{tot}$ (kJ/mol)
MOD5:2	CC-6	$Mn_{\frac{1}{5}}Co_{\frac{1}{5}}Mg_{\frac{1}{5}}Zn_{\frac{1}{5}}Cu_{\frac{1}{5}}$	$Mn_{\frac{1}{2}}Co_{\frac{1}{2}}$	8.99	1.36	1.28	-341.6
MOD6:4	CC-7	$Mn_{\frac{1}{6}}Co_{\frac{1}{6}}Zn_{\frac{1}{6}}Cu_{\frac{1}{6}}Mg_{\frac{1}{6}}Fe_{\frac{1}{6}}$	$Mn_{\frac{1}{4}}Co_{\frac{1}{4}}Fe_{\frac{1}{4}}Al_{\frac{1}{4}}$	7.91	1.19	1.96	-182.6

Dealing with CCSO's, ΔS_{mix}^c can be rescaled to the total number of atoms (*i.e.*, 7 in AB_2O_4), or cations (*i.e.*, 3 in AB_2O_4). The two are therefore linked through the simple relation:

$$\Delta S_{mix}^{cat} = \frac{7}{3}\Delta S_{mix}^{at} \qquad (4)$$

According to references [5,8,10,72,106,107], among the possible metrics to compare entropy in CC materials with multiple cations distributed on different cation sublattices, the cation-driven rescaling is considered the most reliable one, with ΔS_{mix}^{at} defined as

$$\Delta S_{mix}^{at} = -R \left(\frac{\sum_{x=1}^{\bar{x}} b_x \sum_{n=1}^{\bar{N}} \left(f_i^x lnf_i^x\right)}{\sum_{x=1}^{\bar{x}} b_x} \right) \qquad (5)$$

Here b_x is the number of sites on the x sublattice, f_i^x is the fraction of elemental species randomly distributed on the respective sublattice, and $\bar{N}$ is the number of elements in each sublattice. For the generic spinel oxide, Eq. (5) can be rearranged as follows:

$$\Delta S_{mix}^{at} = -\frac{R}{7} \left\{ \left[\sum_{n_1=1}^{N_1} \left(f_{n_1} lnf_{n_1}\right)_{t_h}\right] + \left[2 \cdot \sum_{n_2=1}^{N_2} \left(f_{n_2} lnf_{n_2}\right)_{o_h}\right] + \left[4 \cdot \sum_{n_3=1}^{N_3} \left(f_{n_3} lnf_{n_3}\right)_{O}\right] \right\} \qquad (6)$$

For a stoichiometric oxygen content (*i.e.*, $f_{n_3}=1$), the contribution from the oxygen sublattice is null. ΔS_{mix}^{cat} is plotted in Fig. 8, with values calculated under the assumption of an equimolar distribution in the sublattice (*i.e.*, $f_{n_1}=1/N_1$, $f_{n_2}=1/N_2$, and $f_{n3}=1$). In this sense, they represent the maximum achievable values assuming complete randomization. For comparison, also report ΔS_{mix}^{cat} for a RS structure ($f_{n_2}=0$) filled by N_C different species.

The ideal value of ΔS_{mix}^{cat} obtained from Eqs. 4 and 5 is 1.96 R for MOD6:4. The competing phase of M_3O_4 spinel is its relative MO rock-salt structure. Regarding composition CC-7, signs of a minor RS precipitated phase from the hosting SO matrix start to become apparent at 1473 K, as suggested by the presence of faint RS features in the *ex situ* pattern of CC-7–1473 K (see Fig. 6). The RS phase in Fig. 6 is likely an early seed of a multi-cation rock-salt structure, with Cu and Co being the most abundant cations (Figure S4 and S5). In this respect, the as-synthesized main hosting SO matrix in CC-7–1473 K may seemingly be in close energetic competition with any number of partially/fully ordered states. Consequently, samples presumed to have an ideally randomized distribution of elements may instead exhibit clustering, short-range ordering or site selectivity. The occurrence of clustering or precipitation would generally suggest that ΔS_{mix}^c is insufficient to overcome ΔH_{mix} for at least one species in the mix, making it partly insoluble and resulting in macroscopic phase separation. A similar situation occurs in the prototypal RS (Mg,Co,Ni,Cu,Zn)O wherein synthesis at either too high or too low temperature (compared to T_C) results in clustering and segregation of CuO [105,107] or Cu_2O [108].

Under the hypothesis that ΔS_{mix}^c is the dominating term for the entropy of formation ΔS_f of a solid solution [3,7,9], we can then estimate ΔG_f for CC-7–1473 K as

$$\Delta G_f = CSFE_{tot} - T\Delta S_{mix}^c \qquad (7)$$

and therefore, calculate T_C, i.e., the temperature above which the Gibbs free energy of formation becomes negative. Adopting the values reported in Table 5 for MOD6:4, T_C surpasses 1600 K. On one hand, this is in disagreement with the experimental temperatures observed in the DSC experiment (see Figure 5) and in-situ XRPD (*i.e.*, Fig. 3 and Fig. 4). The sum of the heat exchanged during the two main endothermic reactions P_2 and P_3 amounts to a ΔH_f value of about 88 kJ/mol. As a result, the temperature interval where ΔG_f becomes negative is in better agreement with the experimental evidence, leading to a value of $T_C \cong$ 780 K. As a result, partial spinel inversion could be responsible for the different ΔH_f obtained from CFSE and DSC (see Table S5). In particular, differentiating the distribution of 2+ and 3+ cations in MOD6:4 to the new arrangement $\left(Mn_{1/6}^{3+}Co_{1/6}^{3+}Fe_{1/6}^{3+}Mg_{1/6}^{2+}Zn_{1/6}^{2+}Cu_{1/6}^{2+}\right)_1^{[t_d]}\left(Mn_{1/4}^{2+}Co_{1/4}^{2+}Fe_{1/4}^{3+}Al_{1/4}^{3+}\right)_2^{[o_h]}O_4$, we obtain a value of $CFSE_{TOT} = -100.6$ kJ/mol, corresponding 885 K, relative to an entropy of 1.97 R. Therefore, a T_C which aligns more closely with the one indicated by our DSC data becomes plausible when we assume a small reduction in ΔS_{mix}^{cat} with respect to the ideal value.

A certain degree of inversion (γ) can impact the XRPD patterns, owing to the change in specific site-dependent intensities (*e.g.*, 220 and 111 for t_d-sites and 311 for o_h sites). In the case at hand, different Rietveld refinements made on non-inverted ($\gamma=0$) or fully inverted ($\gamma=1$) models of CC-7–1473 K, resulted in negligible differences in R_{wp} and *g.o.f.* and both models are thus equally acceptable. The type, proportion, and arrangement of cations within the two sublattices have a far greater impact on the resulting powder pattern. As such, while diffraction analysis can effectively validate specific models, it may not conclusively detect the presence of some degree of inversion in multi-element spinels like CC-7–1473 K or CC-6–1273 K. General considerations based on the comparison between simple thermodynamic calculations and in-situ sXRPD and DSC/TGA experiments are more conclusive about the degree of inversion. In summary, MOD6:4 represents the best among the explored models in describing the data. Assuming the validity of this model, we hypothesize that CC-7–1473 K is entropy-stabilized, as discussed earlier, and also high-entropy. At the same time, a certain degree of inversion would explain the lower enthalpic barrier and T_c suggested by our data. The favorable stability conditions achieved for CC-7 have not been met for CC-6, which only shows stability in a narrower range. Assuming the validity of MOD5:2 in describing CC-6–1273 K (*cfr.* Table 4), a configurational entropy boost of 1.28 R makes it stable below 1273 K. Using the $CFSE_{TOT}$ value calculated for MOD5:2 (Table 4) we note that the enthalpic barrier is no less than that acting in MOD6:4. Therefore, for temperatures higher than 1273 K, MOD5:2 would still possess negative ΔG_f, but not enough to overcome the competing RS phase leading to the destabilization of CC-6.

5. Conclusion

In this work, we aimed to create a series of novel Ni- and Cr-free compositionally complex spinel-oxides by combining a progressive number of different cations, ranging from five to seven. This process involved maintaining equal proportions of cations or selectively arranging them within the octahedral and tetrahedral sublattices using the principle of incremental doping. Of the obtained materials three resulted in single-phase spinel-oxides (CC-1, CC-6, and CC-7), with one of them (CC-7) exhibiting thermodynamic stability at temperatures as high as 1473 K. We studied its formation in-situ using synchrotron diffraction to describe phase evolution and formation of intermediates and combined these results to DSC and *ex-situ* diffraction to demonstrate entropy stabilization. The unprecedented stability was obtained through entropy stabilization effect and the resulting seven-cations material, $(Co, Mn, Fe, Cu, Zn, Al, Mg)_3O_4$, can be classified as high-entropy.

CRediT authorship contribution statement

F. Monteverde: Conceptualization, Formal analysis, Funding acquisition, Investigation, Methodology, Project administration, Resources, Validation, Visualization, Writing – original draft, Writing – review & editing. **M. Gaboardi:** Data curation, Formal analysis, Investigation, Methodology, Resources, Validation, Visualization, Writing – original draft, Writing – review & editing.

Declaration of Competing Interest

Acknowledgements

Appendix A. Supporting information

Supplementary data associated with this article can be found in the online version at doi:10.1016/j.jeurceramsoc.2024.05.028.

References

[1] B. Cantor, Multicomponent and high entropy alloys, Entropy 16 (2014) 4749–4768, https://doi.org/10.3390/e16094749.

[2] S. Divilov, H. Eckert, D. Hicks, C. Oses, C. Toher, R. Friedrich, M. Esters, M. J. Mehl, A.C. Zettel, Y. Lederer, E. Zurek, J.-P. Maria, D.W. Brenner, X. Campilongo, S. Filipović, W.G. Fahrenholtz, C.J. Ryan, C.M. DeSalle, R. J. Crealese, D.E. Wolfe, A. Calzolari, S. Curtarolo, Disordered enthalpy–entropy descriptor for high-entropy ceramics discovery, Nature 625 (2024) 66–73, https://doi.org/10.1038/s41586-023-06786-y.

[3] B. Cantor, Multicomponent high-entropy Cantor alloys, Prog. Mater. Sci. 120 (2021), https://doi.org/10.1016/j.pmatsci.2020.100754.

[4] G.N. Kotsonis, S.S.I. Almishal, F. Marques dos Santos Vieira, V.H. Crespi, I. Dabo, C.M. Rost, J. Maria, High-entropy oxides: harnessing crystalline disorder for emergent functionality, J. Am. Ceram. Soc. 106 (2023) 5587–5611, https://doi. org/10.1111/jace.19252.

[5] M. Brahlek, M. Gazda, V. Keppens, A.R. Mazza, S.J. McCormack, A. Mielewczyk-Gryń, B. Musico, K. Page, C.M. Rost, S.B. Sinnott, C. Toher, T.Z. Ward, A. Yamamoto, What is in a name: defining "high entropy" oxides, APL Mater. 10 (2022) 110902, https://doi.org/10.1063/5.0122727.

[6] M. Gaboardi, F. Monteverde, F. Saraga, G. Aquilanti, L. Feng, W. Fahrenholtz, G. Hilmas, Local structure in high-entropy transition metal diborides, Acta Mater. 239 (2022) 118294, https://doi.org/10.1016/j.actamat.2022.118294.

[7] C.M. Rost, Z. Rak, D.W. Brenner, J. Maria, Local structure of the Mg x Ni x Co x Cu x Zn x O(x =0.2) entropy-stabilized oxide: an EXAFS study, J. Am. Ceram. Soc. 100 (2017) 2732–2738, https://doi.org/10.1111/jace.14756.

[8] S.J. McCormack, A. Navrotsky, Thermodynamics of high entropy oxides, Acta Mater. 202 (2021) 1–21, https://doi.org/10.1016/j.actamat.2020.10.043.

[9] B.L. Musicó, D. Gilbert, T.Z. Ward, K. Page, E. George, J. Yan, D. Mandrus, V. Keppens, The emergent field of high entropy oxides: design, prospects, challenges, and opportunities for tailoring material properties, APL Mater. 8 (2020) 040912, https://doi.org/10.1063/5.0003149.

[10] S.S. Aamlid, M. Oudah, J. Rottler, A.M. Hallas, Understanding the role of entropy in high entropy oxides, J. Am. Chem. Soc. 145 (2023) 5991–6006, https://doi. org/10.1021/jacs.2c11608.

[11] J. Gild, T. Harrington, S. Jiang, T. Hu, M.C. Quinn, W.M. Mellor, N. Zhou, K. Vecchio, J. Luo, High-entropy metal diborides: a new class of high-entropy materials and a new type of ultrahigh temperature ceramics, Sci. Rep. 6 (2016) 37946, https://doi.org/10.1038/srep37946.

[12] A.J. Wright, J. Luo, A step forward from high-entropy ceramics to compositionally complex ceramics: a new perspective, J. Mater. Sci. 55 (2020) 9812–9827, https://doi.org/10.1007/s10853-020-04583-w.

[13] F. Wang, F. Monteverde, B. Cui, Will high-entropy carbides and borides be enabling materials for extreme environments? Int. J. Extrem. Manuf. 5 (2023) 022002 https://doi.org/10.1088/2631-7990/acbd6e.

[14] L. Feng, W.G. Fahrenholtz, D.W. Brenner, High-entropy ultra-high-temperature borides and carbides: a new class of materials for extreme environments, Annu Rev. Mater. Res. 51 (2021) 165–185, https://doi.org/10.1146/annurev-matsci-080819-121217.

[15] F. Monteverde, F. Saraga, M. Gaboardi, L. Feng, G. Hilmas, W. Fahrenholtz, Quantitative inspection of grain-scale chemical inhomogeneities in high-entropy AlB 2 -type transition metal diborides, J. Am. Ceram. Soc. 105 (2022) 6910–6923, https://doi.org/10.1111/jace.18619.

[16] L. Feng, F. Monteverde, W.G. Fahrenholtz, G.E. Hilmas, Superhard high-entropy AlB2-type diboride ceramics, Scr. Mater. 199 (2021) 113855, https://doi.org/ 10.1016/j.scriptamat.2021.113855.

[17] T.J. Harrington, J. Gild, P. Sarker, C. Toher, C.M. Rost, O.F. Dippo, C. McElfresh, K. Kaufmann, E. Marin, L. Borowski, P.E. Hopkins, J. Luo, S. Curtarolo, D. W. Brenner, K.S. Vecchio, Phase stability and mechanical properties of novel high entropy transition metal carbides, Acta Mater. 166 (2019) 271–280, https://doi. org/10.1016/j.actamat.2018.12.054.

[18] D.G. Sangiovanni, K. Kaufmann, K. Vecchio, Valence electron concentration as key parameter to control the fracture resistance of refractory high-entropy carbides, Sci. Adv. 9 (2023), https://doi.org/10.1126/sciadv.adi2960.

[19] P. Sarker, T. Harrington, C. Toher, C. Oses, M. Samiee, J.-P. Maria, D.W. Brenner, K.S. Vecchio, S. Curtarolo, High-entropy high-hardness metal carbides discovered by entropy descriptors, Nat. Commun. 9 (2018) 4980, https://doi.org/10.1038/ s41467-018-07160-7.

[20] R.-Z. Zhang, M.J. Reece, Review of high entropy ceramics: design, synthesis, structure and properties, J. Mater. Chem. A Mater. 7 (2019) 22148–22162, https://doi.org/10.1039/C9TA05698J.

[21] O.F. Dippo, N. Mesgarzadeh, T.J. Harrington, G.D. Schrader, K.S. Vecchio, Bulk high-entropy nitrides and carbonitrides, Sci. Rep. 10 (2020) 21288, https://doi. org/10.1038/s41598-020-78175-8.

[22] J. Guan, Y. Liu, D. Li, Z. Yang, S. Qin, D. Jia, Y. Zhou, The new complex high-entropy metal boron carbonitride: microstructure and mechanical properties, J. Am. Ceram. Soc. 105 (2022) 6417–6426, https://doi.org/10.1111/jace.18577.

[23] Y. Wang, T. Csanádi, H. Zhang, J. Dusza, M.J. Reece, Synthesis, microstructure, and mechanical properties of novel high entropy carbonitrides, Acta Mater. 231 (2022) 117887, https://doi.org/10.1016/j.actamat.2022.117887.

[24] J.W. Sturman, E.A. Baranova, Y. Abu-Lebdeh, Review: high-entropy materials for lithium-ion battery electrodes, Front Energy Res. 10 (2022), https://doi.org/ 10.3389/fenrg.2022.862551.

[25] Y. Gao, Y. Liu, H. Yu, D. Zou, High-entropy oxides for catalysis: status and perspectives, Appl. Catal. A Gen. 631 (2022) 118478, https://doi.org/10.1016/j. apcata.2022.118478.

[26] Q. Zhao, Z. Yan, C. Chen, J. Chen, Spinels: controlled preparation, oxygen reduction/evolution reaction application, and beyond, Chem. Rev. 117 (2017) 10121–10211, https://doi.org/10.1021/acs.chemrev.7b00051.

[27] B. Petrovičovà, W. Xu, M.G. Musolino, F. Pantò, S. Patanè, N. Pinna, S. Santangelo, C. Triolo, High-entropy spinel oxides produced via sol-gel and electrospinning and their evaluation as anodes in Li-ion batteries, Appl. Sci. 12 (2022) 5965, https://doi.org/10.3390/app12125965.

[28] H. Minouei, N. Tsvetkov, M. Kheradmandfard, J. Han, D.-E. Kim, S.I. Hong, Tuning the electrochemical performance of high-entropy oxide nanopowder for anode Li-ion storage via structural tailoring, J. Power Sources 549 (2022) 232041, https://doi.org/10.1016/j.jpowsour.2022.232041.

[29] S. LI, Z. PENG, X. FU, Zn 0.5 Co 0.5 Mn 0.5 Fe 0.5 Al 0.5 Mg 0.5 O 4 high-entropy oxide with high capacity and ultra-long life for Li-ion battery anodes, J. Adv. Ceram. 12 (2023) 59–71, https://doi.org/10.26599/JAC.2023.9220666.

[30] W. Bian, H. Li, Z. Zhao, H. Dou, X. Cheng, X. Wang, Entropy stabilization effect and oxygen vacancy in spinel high-entropy oxide promoting sodium ion storage, Electro Acta 447 (2023) 142157, https://doi.org/10.1016/j. electacta.2023.142157.

[31] X.L. Wang, E.M. Jin, G. Sahoo, S.M. Jeong, High-entropy metal oxide (NiMnCrCoFe)3O4 anode materials with controlled morphology for high-performance lithium-ion batteries, Batteries 9 (2023) 147, https://doi.org/ 10.3390/batteries9030147.

[32] D.O. Bayraktar, E. Lökçü, C. Ozgur, T. Erdil, C. Toparli, Effect of synthesis environment on the electrochemical properties of (<scp>FeMnCrCoZn</scp>) <scp> 3 O 4 </scp> high-entropy oxides for Li-ion batteries, Int. J. Energy Res. 46 (2022) 22124–22133, https://doi.org/10.1002/er.8749.

[33] B. Xiao, G. Wu, T. Wang, Z. Wei, Z. Xie, Y. Sui, J. Qi, F. Wei, X. Zhang, L. Tang, J. Zheng, Enhanced Li-Ion diffusion and cycling stability of Ni-free high-entropy spinel oxide anodes with high-concentration oxygen vacancies, ACS Appl. Mater. Interfaces 15 (2023) 2792–2803, https://doi.org/10.1021/acsami.2c12374.

[34] L. Qian, J. Li, G. Lan, Y. Wang, S. Cao, L. Bai, R. Zheng, Z. Wang, S.K. Bhargava, H. Sun, H. Arandiyan, Y. Liu, Towards low-voltage and high-capacity conversion-based oxide anodes by configuration entropy optimization, ChemElectroChem 10 (2023), https://doi.org/10.1002/celc.202201012.

[35] L. Dong, Z. Wang, Y. Li, C. Jin, F. Dong, W. Zhao, C. Qin, Z. Wang, Spinel-structured, multi-component transition metal oxide (Ni,Co,Mn)Fe2O4−x as long-life lithium-ion battery anode material, Batteries 9 (2023) 54, https://doi.org/ 10.3390/batteries9010054.

[36] X. Liu, X. Li, Y. Li, H. Zhang, Q. Jia, S. Zhang, W. Lei, High-entropy oxide: a future anode contender for lithium-ion battery, EcoMat 4 (2022), https://doi.org/ 10.1002/eom2.12261.

[37] T.X. Nguyen, C.-C. Tsai, J. Patra, O. Clemens, J.-K. Chang, J.-M. Ting, Co-free high entropy spinel oxide anode with controlled morphology and crystallinity for outstanding charge/discharge performance in Lithium-ion batteries, Chem. Eng. J. 430 (2022) 132658, https://doi.org/10.1016/j.cej.2021.132658.

[38] Z. Sun, Y. Zhao, C. Sun, Q. Ni, C. Wang, H. Jin, High entropy spinel-structure oxide for electrochemical application, Chem. Eng. J. 431 (2022) 133448, https:// doi.org/10.1016/j.cej.2021.133448.

[39] X. Luo, J. Patra, W. Chuang, T.X. Nguyen, J. Ting, J. Li, C. Pao, J. Chang, Charge–discharge mechanism of high-entropy Co-free spinel oxide toward Li + storage examined using operando quick-scanning X-ray absorption spectroscopy, Adv. Sci. 9 (2022) 2201219, https://doi.org/10.1002/advs.202201219.

[40] Y. Xu, X. Xu, L. Bi, A high-entropy spinel ceramic oxide as the cathode for proton-conducting solid oxide fuel cells, J. Adv. Ceram. 11 (2022) 794–804, https://doi.org/10.1007/s40145-022-0573-7.

[41] B. Xiao, G. Wu, T. Wang, Z. Wei, Y. Sui, B. Shen, J. Qi, F. Wei, Q. Meng, Y. Ren, X. Xue, J. Zheng, J. Mao, K. Dai, High entropy oxides (FeNiCrMnX)3O4 (X=Zn, Mg) as anode materials for lithium ion batteries, Ceram. Int. 47 (2021) 33972–33977, https://doi.org/10.1016/j.ceramint.2021.08.303.

[42] B. Xiao, G. Wu, T. Wang, Z. Wei, Y. Sui, B. Shen, J. Qi, F. Wei, J. Zheng, High-entropy oxides as advanced anode materials for long-life lithium-ion batteries, Nano Energy 95 (2022) 106962, https://doi.org/10.1016/j.nanoen.2022.106962.

[43] J. Patra, T.X. Nguyen, C. Tsai, O. Clemens, J. Li, P. Pal, W.K. Chan, C. Lee, H.T. Chen, J. Ting, J. Chang, Effects of elemental modulation on phase purity and electrochemical properties of Co-free high-entropy spinel oxide anodes for lithium-ion batteries, Adv. Funct. Mater. 32 (2022) 2110992, https://doi.org/10.1002/adfm.202110992.

[44] N. Sreenivasulu, U.N. Kumar, K.M.V.V. Madhav, T. Thomas, S.S. Bhattacharya, Structural and electrochemical investigations on nanocrystalline high entropy spinel oxides for battery-like supercapacitor applications, ChemistrySelect 7 (2022), https://doi.org/10.1002/slct.202104015.

[45] J. Zhao, X. Yang, Y. Huang, F. Du, Y. Zeng, Entropy stabilization effect and oxygen vacancies enabling spinel oxide highly reversible lithium-ion storage, ACS Appl. Mater. Interfaces 13 (2021) 58674–58681, https://doi.org/10.1021/acsami.1c18362.

[46] X. Yang, H. Wang, Y. Song, K. Liu, T. Huang, X. Wang, C. Zhang, J. Li, Low-temperature synthesis of a porous high-entropy transition-metal oxide as an anode for high-performance lithium-ion batteries, ACS Appl. Mater. Interfaces 14 (2022) 26873–26881, https://doi.org/10.1021/acsami.2c07576.

[47] Q. Dong, M. Hong, J. Gao, T. Li, M. Cui, S. Li, H. Qiao, A.H. Brozena, Y. Yao, X. Wang, G. Chen, J. Luo, L. Hu, Rapid synthesis of high-entropy oxide microparticles, Small 18 (2022) 2104761, https://doi.org/10.1002/smll.202104761.

[48] H. Chen, N. Qiu, B. Wu, Z. Yang, S. Sun, Y. Wang, A new spinel high-entropy oxide (Mg 0.2 Ti 0.2 Zn 0.2 Cu 0.2 Fe 0.2) 3 O 4 with fast reaction kinetics and excellent stability as an anode material for lithium ion batteries, RSC Adv. 10 (2020) 9736–9744, https://doi.org/10.1039/D0RA00255K.

[49] Y. Zheng, X. Wu, X. Lan, R. Hu, A Spinel (FeNiCrMnMgAl)3O4 high entropy oxide as a cycling stable anode material for Li-ion batteries, Processes 10 (2021) 49, https://doi.org/10.3390/pr10010049.

[50] K.-H. Tian, C.-Q. Duan, Q. Ma, X.-L. Li, Z.-Y. Wang, H.-Y. Sun, S.-H. Luo, D. Wang, Y.-G. Liu, High-entropy chemistry stabilizing spinel oxide (CoNiZnXMnLi)3O4 (X = Fe, Cr) for high-performance anode of Li-ion batteries, Rare Met. 41 (2022) 1265–1275, https://doi.org/10.1007/s12598-021-01872-4.

[51] M. Moździerz, K. Świerczek, J. Dąbrowa, M. Gajewska, A. Hanc, Z. Feng, J. Cieślak, M. Kądziołka-Gaweł, J. Płotek, M. Marzec, A. Kulka, High-entropy Sn 0.8 (Co 0.2 Mg 0.2 Mn 0.2 Ni 0.2 Zn 0.2) 2.2 O 4 conversion-alloying anode material for Li-ion cells: altered lithium storage mechanism, activation of Mg, and origins of the improved cycling stability, ACS Appl. Mater. Interfaces 14 (2022) 42057–42070, https://doi.org/10.1021/acsami.2c11038.

[52] C. Duan, K. Tian, X. Li, D. Wang, H. Sun, R. Zheng, Z. Wang, Y. Liu, New spinel high-entropy oxides (FeCoNiCrMnXLi)3O4 (X = Cu, Mg, Zn) as the anode material for lithium-ion batteries, Ceram. Int. 47 (2021) 32025–32032, https://doi.org/10.1016/j.ceramint.2021.08.091.

[53] C. Triolo, M. Maisuradze, M. Li, Y. Liu, A. Ponti, G. Pagot, V. Di Noto, G. Aquilanti, N. Pinna, M. Giorgetti, S. Santangelo, Charge storage mechanism in electrospun spinel-structured high-entropy (Mn 0.2 Fe 0.2 Co 0.2 Ni 0.2 Zn 0.2) 3 O 4 oxide nanofibers as anode material for Li-ion batteries, Small 19 (2023), https://doi.org/10.1002/smll.202304585.

[54] A. Mao, H.-X. Xie, H.-Z. Xiang, Z.-G. Zhang, H. Zhang, S. Ran, A novel six-component spinel-structure high-entropy oxide with ferrimagnetic property, J. Magn. Magn. Mater. 503 (2020) 166594, https://doi.org/10.1016/j.jmmm.2020.166594.

[55] X. Sun, X. Zeng, X. He, W. Fang, X. Du, W. Li, L. Zhao, H. Chen, Influence of oxygen vacancies on the structure and magnetic properties of high entropy (Co, Cr,Fe,Mn,Ni)3O4 ceramics, J. Alloy. Compd. 925 (2022) 166560, https://doi.org/10.1016/j.jallcom.2022.166560.

[56] Z. Jiang, R. Zhang, H. Zhao, J. Wang, L. Jia, Y. Hu, K. Wang, X. Wang, Preparation of (Ga0.2Cr0.2Mn0.2Ni0.2Zn0.2)3O4 high-entropy oxide with narrow bandgap for photocatalytic CO2 reduction with water vapor, Appl. Surf. Sci. 612 (2023) 155809, https://doi.org/10.1016/j.apsusc.2022.155809.

[57] A.K. Gupta, P. Kumari, A. Prakash, N.K. Giri, R.R. Shahi, Synthesis, characterizations, and magnetic behavior of novel (CuNiTiZnFe)3O4 high entropy spinel oxide, Ceram. Int. 48 (2022) 36258–36263, https://doi.org/10.1016/j.ceramint.2022.08.183.

[58] S.K. Shaw, P. Kumari, A. Sharma, N. Jatav, A. Gangwar, N.S. Anuraag, P. Rajput, S. Kavita, S.S. Meena, M. Vasundhara, I. Sinha, N.K. Prasad, Assessment of ionic site distributions in magnetic high entropy oxide of (Mn0·2Fe0·2Co0·2Ni0·2Zr0.2)3O4 and its catalytic behaviour, Phys. B Condens Matter 652 (2023) 414653, https://doi.org/10.1016/j.physb.2023.414653.

[59] A. Mohan, V. Hastak, A.S. Gandhi, Design and synthesis of a stable multicomponent equimolar high entropy oxide with spinel structure, Mater. 20 (2021) 101259, https://doi.org/10.1016/j.mtla.2021.101259.

[60] Y. Wang, H. Li, H. Liu, L. Yang, C. Zeng, Preparation and formation mechanism of Cr-free spinel-structured high entropy oxide (MnFeCoNiCu)3O4, Ceram. Int. 49 (2023) 1940–1946, https://doi.org/10.1016/j.ceramint.2022.09.159.

[61] M. Fracchia, M. Manzoli, U. Anselmi-Tamburini, P. Ghigna, A new eight-cation inverse high entropy spinel with large configurational entropy in both tetrahedral and octahedral sites: synthesis and cation distribution by X-ray absorption spectroscopy, Scr. Mater. 188 (2020) 26–31, https://doi.org/10.1016/j.scriptamat.2020.07.002.

[62] X. Wang, B.L. Musicó, C. Kons, P.C. Metz, V. Keppens, D.A. Gilbert, Y. Zhang, K. Page, Local cation order and ferrimagnetism in compositionally complex spinel ferrites, APL Mater. 10 (2022) 121102, https://doi.org/10.1063/5.0123728.

[63] A. Ponti, C. Triolo, B. Petrovičovà, A.M. Ferretti, G. Pagot, W. Xu, V. Di Noto, N. Pinna, S. Santangelo, Structure and magnetism of electrospun porous high-entropy (Cr 1/5 Mn 1/5 Fe 1/5 Co 1/5 Ni 1/5) 3 O 4, (Cr 1/5 Mn 1/5 Fe 1/5 Co 1/5 Zn 1/5) 3 O 4 and (Cr 1/5 Mn 1/5 Fe 1/5 Ni 1/5 Zn 1/5) 3 O 4 spinel oxide nanofibers, Phys. Chem. Chem. Phys. 25 (2023) 2212–2226, https://doi.org/10.1039/D2CP05142G.

[64] X. Liu, X. Wang, H. Sun, Z. Zhang, P. Song, Y. Liu, Highly stable bimetal Ni–Co on alumina-covered spinel oxide derived from high entropy oxide for CO 2 methanation, Ind. Eng. Chem. Res. 62 (2023) 341–354, https://doi.org/10.1021/acs.iecr.2c03876.

[65] C. Duan, X. Li, D. Wang, Z. Wang, H. Sun, R. Zheng, Y. Liu, Nanosized high entropy spinel oxide (FeCoNiCrMn) 3 O 4 as a highly active and ultra-stable electrocatalyst for the oxygen evolution reaction, Sustain Energy Fuels 6 (2022) 1479–1488, https://doi.org/10.1039/D1SE02038B.

[66] J. Massoudi, O. Messaoudi, S. Gharbi, T. Mnasri, E. Dhahri, K. Khirouni, E.K. Hlil, L. Alfhaid, L. Manai, A. Azhary, Magnetocaloric effect, dielectric relaxor behavior, and evidence for direct magnetodielectric behavior in Ni 0.6 Zn 0.4 Al 0.5 Fe 1.5 O 4 ceramics for high-temperature applications, J. Phys. Chem. C 126 (2022) 2857–2867, https://doi.org/10.1021/acs.jpcc.1c09838.

[67] A.H. Phakatkar, M.T. Saray, M.G. Rasul, L.V. Sorokina, T.G. Ritter, T. Shokuhfar, R. Shahbazian-Yassar, Ultrafast synthesis of high entropy oxide nanoparticles by flame spray pyrolysis, Langmuir 37 (2021) 9059–9068, https://doi.org/10.1021/acs.langmuir.1c01105.

[68] T. Parida, A. Karati, K. Guruvidyathri, B.S. Murty, G. Markandeyulu, Novel rare-earth and transition metal-based entropy stabilized oxides with spinel structure, Scr. Mater. 178 (2020) 513–517, https://doi.org/10.1016/j.scriptamat.2019.12.027.

[69] B.L. Musicó, J.P. Smith, Q. Wright, K. Sickafus, D.G. Mandrus, V. Keppens, Synthesis, elastic properties, and high-temperature stability of multicomponent spinel oxide, MRS Commun. 12 (2022) 723–728, https://doi.org/10.1557/s43579-022-00210-8.

[70] B. Wang, J. Yao, P. Zhao, J. Wang, A. Chang, A comparative study of different oxidation states of raw materials on the properties of a novel medium-entropy Co2.77Mn1.71Fe1.10Zn0.42O8 thermistor materials, Mater. Chem. Phys. 284 (2022) 126018, https://doi.org/10.1016/j.matchemphys.2022.126018.

[71] H.-X. Guo, W.-M. Wang, C.-Y. He, B.-H. Liu, D.-M. Yu, G. Liu, X.-H. Gao, Entropy-assisted high-entropy oxide with a spinel structure toward high-temperature infrared radiation materials, ACS Appl. Mater. Interfaces 14 (2022) 1950–1960, https://doi.org/10.1021/acsami.1c20055.

[72] A. Sarkar, B. Eggert, R. Witte, J. Lill, L. Velasco, Q. Wang, J. Sonar, K. Ollefs, S. S. Bhattacharya, R.A. Brand, H. Wende, F.M.F. de Groot, O. Clemens, H. Hahn, R. Kruk, Comprehensive investigation of crystallographic, spin-electronic and magnetic structure of Co0.2Cr0.2Fe0.2Mn0.2Ni0.2)3O4 Unraveling the suppression of configuration entropy in high entropy oxides, Acta Mater. 226 (2022) 117581, https://doi.org/10.1016/j.actamat.2021.117581.

[73] J.X. Yang, B.-H. Dai, C.-Y. Chiang, I.-C. Chiu, C.-W. Pao, S.-Y. Lu, I.-Y. Tsao, S.-T. Lin, C.-T. Chiu, J.-W. Yeh, P.-C. Chang, W.-H. Hung, Rapid fabrication of high-entropy ceramic nanomaterials for catalytic reactions, ACS Nano 15 (2021) 12324–12333, https://doi.org/10.1021/acsnano.1c04259.

[74] B. Wang, J. Yao, J. Wang, A. Chang, Spinel-type high-entropy (Co0.2Mn0.2Fe0.2Zn0.2Ti0.2)3O4 oxides constructed from disordered cations and oxygen vacancies, J. Alloy. Compd. 897 (2022) 163188, https://doi.org/10.1016/j.jallcom.2021.163188.

[75] B. Talluri, K. Yoo, J. Kim, High entropy spinel metal oxide (CoCrFeMnNi)3O4 nanoparticles as novel efficient electrocatalyst for methanol oxidation and oxygen evolution reactions, J. Environ. Chem. Eng. 10 (2022) 106932, https://doi.org/10.1016/j.jece.2021.106932.

[76] J. Ma, B. Zhao, H. Xiang, F.-Z. Dai, Y. Liu, R. Zhang, Y. Zhou, High-entropy spinel ferrites MFe2O4 (M = Mg, Mn, Fe, Co, Ni, Cu, Zn) with tunable electromagnetic properties and strong microwave absorption, J. Adv. Ceram. 11 (2022) 754–768, https://doi.org/10.1007/s40145-022-0569-3.

[77] S.L. Fereja, Z. Zhang, Z. Fang, J. Guo, K. Liu, Z. Li, W. Chen, High-entropy oxide derived from metal–organic framework as a bifunctional electrocatalyst for efficient urea oxidation and oxygen evolution reactions, ACS Appl. Mater. Interfaces 14 (2022) 38727–38738, https://doi.org/10.1021/acsami.2c09161.

[78] S. Nie, L. Wu, L. Zhao, X. Zheng, S. Yang, P. Zhang, Entropy-driven chemistry reveals highly stable denary MgAl2O4-type catalysts, Chem. Catal. 1 (2021) 648–662, https://doi.org/10.1016/j.checat.2021.04.001.

[79] H. Minouei, M. Kheradmandfard, M. Saboktakin Rizi, M. Jalaly, D.-E. Kim, S.I. Hong, Formation mechanism of high-entropy spinel thin film and its mechanical and magnetic properties: linking high-entropy alloy to high-entropy ceramic, Appl. Surf. Sci. 576 (2022) 151719, https://doi.org/10.1016/j.apsusc.2021.151719.

[80] B. Musicó, Q. Wright, T.Z. Ward, A. Grutter, E. Arenholz, D. Gilbert, D. Mandrus, V. Keppens, Tunable magnetic ordering through cation selection in entropic spinel oxides, Phys. Rev. Mater. 3 (2019) 104416, https://doi.org/10.1103/PhysRevMaterials.3.104416.

[81] J. Dąbrowa, M. Stygar, A. Mikuła, A. Knapik, K. Mroczka, W. Tejchman, M. Danielewski, M. Martin, Synthesis and microstructure of the (Co,Cr,Fe,Mn,Ni) 3 O 4 high entropy oxide characterized by spinel structure, Mater. Lett. 216 (2018) 32–36, https://doi.org/10.1016/j.matlet.2017.12.148.

[82] M. Stygar, J. Dąbrowa, M. Moździerz, M. Zajusz, W. Skubida, K. Mroczka, K. Berent, E. Świerczek, M. Danielewski, Formation and properties of high entropy oxides in Co-Cr-Fe-Mg-Mn-Ni-O system: novel (Cr,Fe,Mg,Mn,Ni)3O4 and (Co,Cr,Fe,Mg,Mn)3O4 high entropy spinels, J. Eur. Ceram. Soc. 40 (2020) 1644–1650, https://doi.org/10.1016/j.jeurceramsoc.2019.11.030.

[83] A. Mao, H.-Z. Xiang, Z.-G. Zhang, K. Kuramoto, H. Zhang, Y. Jia, A new class of spinel high-entropy oxides with controllable magnetic properties, J. Magn. Magn. Mater. 497 (2020) 165884, https://doi.org/10.1016/j.jmmm.2019.165884.

[84] A.L.F. Cardoso, C.P.F. Perdomo, B.G. Foschiani, I.C.S. Barbara, J.A. Xaraba, F. L. Zabotto, R.F.K. Gunnewiek, Microwave synthesis of nanostructured high entropy spinel, Mater. Lett. 333 (2023) 133539, https://doi.org/10.1016/j.matlet.2022.133539.

[85] Q. Zhang, Y. Hu, H. Wu, X. Zhao, M. Wang, S. Wang, R. Feng, Q. Chen, F. Song, M. Chen, P. Liu, Entropy-stabilized multicomponent porous spinel nanowires of NiFeXO 4 (X = Fe, Ni, Al, Mo, Co, Cr) for efficient and durable electrocatalytic oxygen evolution reaction in alkaline medium, ACS Nano 17 (2023) 1485–1494, https://doi.org/10.1021/acsnano.2c10247.

[86] M. Kubisztal, Hopping conductivity and low-temperature magnetoresistance of high-entropy (Mn,Fe,Ni,Co,Zn)3O4 polycrystalline ceramics, Ceram. Int. 49 (2023) 19442–19450, https://doi.org/10.1016/j.ceramint.2023.03.073.

[87] M. Einert, A. Waheed, S. Lauterbach, M. Mellin, M. Rohnke, L.Q. Wagner, J. Gallenberger, C. Tian, B.M. Smarsly, W. Jaegermann, F. Hess, H. Schlaad, J. P. Hofmann, Sol-gel-derived ordered mesoporous high entropy spinel ferrites and assessment of their photoelectrochemical and electrocatalytic water splitting performance, Small 19 (2023), https://doi.org/10.1002/smll.202205412.

[88] L. He, H. Kang, G. Hou, X. Qiao, X. Jia, W. Qin, X. Wu, Low-temperature synthesis of nano-porous high entropy spinel oxides with high grain boundary density for oxygen evolution reaction, Chem. Eng. J. 460 (2023) 141675, https://doi.org/10.1016/j.cej.2023.141675.

[89] H. Minouei, M. Jalaly, M. Kheradmandfard, M. Saboktakin Rizi, D.-E. Kim, S. I. Hong, Rapid microwave-assisted synthesis and magnetic properties of high-entropy spinel (Cr0.2Mn0.2Fe0.2Co0.2-Ni Zn)3O4 nanoparticles, Ceram. Int. 49 (2023) 11885–11892, https://doi.org/10.1016/j.ceramint.2022.12.036.

[90] J.M. Gonçalves, A. Ghorbani, T.G. Ritter, I.S. Lima, M. Tamadoni Saray, A. H. Phakatkar, V.D. Silva, R.S. Pereira, A.L. Yarin, I. Angnes, R. Shahbazian-Yassar, Multimetallic glycerolate as a precursor template of spherical porous high-entropy oxide microparticles, J. Colloid Interface Sci. 641 (2023) 643–652, https://doi.org/10.1016/j.jcis.2023.03.089.

[91] R.R. Katzbaer, F.M. dos Santos Vieira, I. Dabo, Z. Mao, R.E. Schaak, Band gap narrowing in a high-entropy spinel oxide semiconductor for enhanced oxygen evolution catalysis, J. Am. Chem. Soc. 145 (2023) 6753–6761, https://doi.org/10.1021/jacs.2c12887.

[92] M. Coduri, M. Fracchia, M. Guerrini, C. Dejoie, P. Ghigna, U.A. Tamburini, Novel In-based high entropy spinel oxides with tunable lattice parameter, J. Eur. Ceram. Soc. 43 (2023) 2728–2739, https://doi.org/10.1016/j.jeurceramsoc.2022.12.047.

[93] S.K. Shaw, P. Kumari, A. Sharma, N. Jatav, A. Gangwar, N.S. Anuraag, P. Rajput, S. Kavita, S.S. Meena, M. Vasundhara, I. Sinha, N.K. Prasad, Assessment of ionic site distributions in magnetic high entropy oxide of

(Mn0·2Fe0·2Co0·2Ni0·2Zr0.2)3O4 and its catalytic behaviour, Phys. B Condens Matter 652 (2023) 414653, https://doi.org/10.1016/j.physb.2023.414653.

[94] P. Amarnath, R. Madhu, K. Praveen, S. Govindarajan, S. Kundu, Y. Subramaniam, Phase-pure high-entropy spinel oxide (Ni,Fe,Mn,Cu,Zn) 3 O 4 via thermal plasma: a promising electrocatalyst for oxygen evolution reaction, ACS Appl. Energy Mater. 6 (2023) 5899–5911, https://doi.org/10.1021/acsaem.3c00311.

[95] J. Ai, Y. Shuai, M. Hu, L. Cheng, S. Luo, W. Li, Z. Chen, L. Hu, Z. Zhou, Microstructural evolution and catalytic properties of novel high-entropy spinel ferrites MFe2O4 (M= Mg, Co, Ni, Cu, Zn), Ceram. Int. 49 (2023) 22941–22951, https://doi.org/10.1016/j.ceramint.2023.04.119.

[96] D. Wang, C. Duan, H. He, Z. Wang, R. Zheng, H. Sun, Y. Liu, C. Liu, Microwave solvothermal synthesis of component-tunable high-entropy oxides as high-efficient and stable electrocatalysts for oxygen evolution reaction, J. Colloid Interface Sci. 646 (2023) 89–97, https://doi.org/10.1016/j.jcis.2023.05.043.

[97] A. Esmaeilzaei, J. Vahdati Khaki, S. abdolkarim Sajjadi, S. Mollazadeh, Synthesis and crystallization of (Co, Cr, Fe, Mn, Ni)3O4 high entropy oxide: the role of fuel and fuel-to-oxidizer ratio, J. Solid State Chem. 321 (2023) 123912, https://doi.org/10.1016/j.jssc.2023.123912.

[98] C.A. Corlett, N. Obradovic, J.L. Watts, E.W. Bohannan, W.G. Fahrenholtz, Synthesis, densification, and cation inversion in high entropy (Co,Cu,Mg,Ni,Zn)Al 2 O 4 spinel, J. Asian Ceram. Soc. 11 (2023) 330–337, https://doi.org/10.1080/21870764.2023.2227535.

[99] Y. Han, M. Tian, C. Wang, T. Zong, X. Wang, High-entropy spinel oxide (Fe0.2Mg0.2Mn0.1Al0.3Cr0.2)3O4 as a highly active and stable redox material for methane driven solar thermochemical water splitting, Appl. Catal. B 339 (2023) 123096, https://doi.org/10.1016/j.apcatb.2023.123096.

[100] P. Riello, A. Lausi, J. Macleod, J.R. Plaisier, G. Zerauschek, P. Fornasiero, In situ reaction furnace for real-time XRD studies, J. Synchrotron Radiat. 20 (2013) 194–196, https://doi.org/10.1107/S0909049512039246.

[101] L. Rebuffi, J.R. Plaisier, M. Abdellatief, A. Lausi, P. Scardi, MCX: a synchrotron radiation beamline for X-ray diffraction line profile analysis, Z. Anorg. Allg. Chem. 640 (2014) 3100–3106, https://doi.org/10.1002/zaac.201400163.

[102] B.H. Toby, R.B. Von Dreele, GSAS-II: the genesis of a modern open-source all purpose crystallography software package, J. Appl. Crystallogr 46 (2013) 544–549, https://doi.org/10.1107/S0021889813003531.

[103] Transactions and Communications, Journal of the Society of Chemical Industry 63 (1944) 125–160. ⟨https://doi.org/10.1002/jctb.5000630501⟩.

[104] F. Monteverde, F. Saraga, M. Gaboardi, L. Feng, G. Hilmas, W. Fahrenholtz, Quantitative inspection of grain-scale chemical inhomogeneities in high-entropy AlB 2 -type transition metal diborides, J. Am. Ceram. Soc. 105 (2022) 6910–6923, https://doi.org/10.1111/jace.18619.

[105] C.M. Rost, D.L. Schmuckler, C. Bumgardner, M.S. Bin Hoque, D.R. Diercks, J. T. Gaskins, J.-P. Maria, G.L. Brennecka, X. Li, P.E. Hopkins, On the thermal and mechanical properties of Mg 0.2 Co 0.2 Ni 0.2 Cu 0.2 Zn 0.2 O across the high-entropy to entropy-stabilized transition, APL Mater. 10 (2022) 121108, https://doi.org/10.1063/5.0122775.

[106] M. Fracchia, M. Coduri, P. Ghigna, U. Anselmi-Tamburini, Phase stability of high entropy oxides: a critical review, J. Eur. Ceram. Soc. (2023), https://doi.org/10.1016/j.jeurceramsoc.2023.09.056.

[107] M. Webb, M. Gerhart, S. Baksa, S. Gelin, A.-R. Ansbro, P.B. Meisenheimer, T. Chiang, J.-P. Maria, I. Dabo, C.M. Rost, J.T. Heron, High temperature stability of entropy-stabilized oxide (MgCoNiCuZn)0.2O in air, Appl. Phys. Lett. 124 (2024), https://doi.org/10.1063/5.0199076.

[108] A.D. Dupuy, X. Wang, J.M. Schoenung, Entropic phase transformation in nanocrystalline high entropy oxides, Mater. Res. Lett. 7 (2019) 60–67, https://doi.org/10.1080/21663831.2018.1554605.